A&A 434, 713–724 (2005)
DOI: 10.1051/0004-6361:20042096

Astronomy & Astrophysics

Scattering polarization in strong chromospheric lines

I. Explanation of the triplet peak structure

R. Holzreuter[1], D. M. Fluri[1], and J. O. Stenflo[1,2]

[1] Institute of Astronomy, ETH Zentrum, 8092 Zurich, Switzerland
[2] Faculty of Mathematics & Science, University of Zurich, 8057 Zurich, Switzerland
e-mail: [holzreuter;fluri;stenflo]@astro.phys.ethz.ch

Received 30 September 2004 / Accepted 23 December 2004

Abstract. Although the triplet polarization structure of the Na I D_2 and Ca I 4227 Å lines in the second solar spectrum has been known for more than two decades, a clear and consistent explanation has been lacking. Here we show that the qualitative profile shape may be explained in terms of the anisotropy of the radiation field and partial frequency redistribution (PRD) effects. The complicated frequency and depth dependence of the anisotropy can be understood in terms of simple arguments that involve the source function gradient and boundary effects. We show in particular that the triplet peak structure of the polarization profile of Na I D_2 has basically the same origin as for the Ca I 4227 Å line. Hyperfine structure and lower-level atomic polarization only modify the core polarization without altering the overall qualitative features.
For our calculations we adopt a numerical method that combines the advantages of both the classical formalism with integral source function and the density-matrix formalism. In a first step, a multi-level, PRD-capable MALI code, which solves the statistical equilibrium and the radiative transfer equation self-consistently, computes intensity, opacities and collision rates. Keeping these quantities fixed, we obtain the scattering polarization in a second step by solving the radiative transfer equation for the transitions of interest with the classical formalism, which assumes a two-level atomic model with unpolarized lower level. Quantum interferences and lower-level atomic polarization are included in terms of a wavelength dependent polarizability W_2, which is independently obtained with the density-matrix formalism.

Key words. line: formation – polarization – radiative transfer – scattering – Sun: atmosphere

1. Introduction

Coherent scattering in the solar atmosphere generates a linearly polarized spectrum, known as the "second solar spectrum" (Ivanov 1991), that consists of a polarized continuum on which depolarizing and intrinsically polarizing lines are superposed. The richly structured second solar spectrum contains a plethora of information complementary to the intensity spectrum (Stenflo & Keller 1996, 1997). The most interesting diagnostic potential of scattering polarization, apart from additional constraints on abundances and thermodynamic properties of the solar atmosphere, is its sensitivity to the Hanle effect in the presence of weak magnetic fields. The Hanle effect is best visible in chromospheric lines, for which spatial variations of the magnetic field are easily resolved with current instruments (see e.g. Stenflo 2002).

Systematic diagnostics is only possible with good observations, a solid theory, and the appropriate numerical tools. The ZIMPOL polarimeter (Povel 1995) enables excellent observations and systematic exploration of the second solar spectrum (Gandorfer 2000, 2002, 2004). However, the development of the theoretical framework has turned out to be rather challenging. The physics underlying coherent scattering involves subtle effects such as quantum interferences between different levels and optical pumping. A self-consistent theory of non-LTE radiative transfer with partial frequency redistribution (PRD) that contains these effects is still missing, although some first steps have been taken (Bommier 1997a,b; Landi Degl'Innocenti et al. 1996).

Strong chromospheric lines are particularly challenging for theoreticians. In general, coherent scattering in a large number of such lines, where the most prominent are the Ca I 4227 Å, the Sr II 4078 Å and the Cr I 3594 Å lines but also a large number of Fe lines (Gandorfer 2000, 2002, 2004), produces linear polarization profiles with a distinct triplet structure. Rees & Saliba (1982) have demonstrated that the polarization wings result from PRD effects and are common to many types of atmospheres even for isothermal models. They used the approximation of PRD proposed by Kneer (1975) and also noticed the close relation between anisotropy variations in the atmosphere and the polarization profile. Detailed theoretical analysis of scattering polarization in non-magnetic atmospheres involving proper PRD has been done by Faurobert (1987, 1988). The first realistic modeling of scattering polarization in

chromospheric lines including collisions and Hanle effect was performed by Faurobert-Scholl (1992) for the Ca I 4227 Å line with the integral formalism of radiative transfer. The author discussed the spectral features in detail and noticed a small dip in the polarization profile at line center, which had not been observed before. However, the line core including this dip was not properly explained. Later, Faurobert-Scholl (1994) proposed canopy like magnetic fields in the lower chromosphere to improve the fit to the observations of the center-to-limb variation of the polarized line cores in Ca I 4227 Å and Sr II 4078 Å.

The above-mentioned integral formalism is a good choice for strong lines with prominent wings but is strictly valid only for two-level model atoms with negligible lower-level atomic polarization. There are many other spectral lines of diagnostic interest, such as Mg I b-lines or the Ca II IR triplet, whose scattering polarization signals, which do not show a triplet peak structure, are mainly due to the presence of atomic polarization in their long-lived lower levels (Trujillo Bueno 2001). The observed Q/I in the Ca II IR triplet has been successfully modeled within the framework of the CRD density-matrix polarization transfer theory by Manso Sainz & Trujillo Bueno (2003). The big advantage of this formalism is the consistent inclusion of all the optical pumping and quantum-interference effects. However, for the strong lines considered in this work, PRD effects are important and the assumption of CRD is not adequate.

One of the greatest challenges for the theory of scattering polarization is presented by the Na I D lines, because they involve PRD effects, quantum interferences between the fine-structure and hyperfine structure levels, and the enigmatic core polarization in D_1. Lacking a self-consistent theory these lines can only be modeled based on approximations. A difficulty is that the classic integral formalism easily accounts for PRD in single lines but cannot deal with quantum interferences and optical pumping, while in the density-matrix formalism the opposite is the case. Nonetheless, using the heuristic PRD approach with metalevels in the density-matrix formalism, Landi Degl'Innocenti (1998, 1999) was able to fit the observed polarization profile when accounting for hyperfine structure and lower-level atomic polarization. The calculations involved ad hoc assumptions such as a very high, constant anisotropy of the radiation field and frequency coherent scattering.

We propose a modeling strategy that combines the advantages of both formalisms, and which allows us to conduct non-LTE radiative transfer with PRD accounting at the same time for quantum interferences and optical pumping. With this tool we intend to study scattering polarization in strong chromospheric lines. In view of the great advances in the observations of scattering polarization there is a growing need to further develop the modeling of such lines. Here we concentrate on a transparent explanation of the triplet peak in the polarization profile and on the identification of the main physical processes involved. Because the emergent polarization scales with the anisotropy of the radiation field we discuss first the frequency and depth dependence of the anisotropy before studying the polarization profiles. As we shall see below, much of the complicated behavior of the anisotropy can be understood in terms of the arguments presented by Trujillo Bueno (2001), which involve the influence of the source function gradient and boundary effects. All our considerations are based on calculations for the Ca I 4227 Å and the Na I D_2 lines, two typical examples of chromospheric lines (Fig. 1). This allows us in particular to clarify the main physical origin of the triplet peak in Na I D_2.

2. Modeling line polarization

The computations have been performed for a plane-parallel model atmosphere, namely model FALC by Fontenla et al. (1993) with zero magnetic field. The modeling is divided into two major modules.

In the first step we compute opacities, intensity and collisional rates neglecting any polarization. We have used a PRD-capable MALI-code (henceforth RH-code) developed by Uitenbroek (2001) to solve the statistical equilibrium equations and the radiative transfer equation self-consistently. PRD-capability, consistent calculation of overlapping lines, and the possibility to include background lines have made this code – based on a formalism of Rybicki & Hummer (1991, 1992) – the preferred choice. The MULTI code (Carlsson 1986) that was previously applied (Fluri et al. 2003) served for testing and comparison. A Ca I model atom with 18 and a Na I atom with 16 levels, the latter provided by Bruls et al. (1992), have been used alternatively in full CRD- or in mixed PRD/CRD-mode of the RH-code.

In the second step the scattering polarization is computed iteratively for the lines considered, assuming that the quantities obtained in the first step (intensity, opacities, collisional rates) are not affected by the polarization. The small degree of polarization of about 1% justifies this assumption very well. We have implemented the equations in the classic formalism with the source function in integral form for a two-level atom whose lower level is assumed to be unpolarized. The total source function is given by

$$\boldsymbol{S}_{\mathrm{tot},x} = \frac{\kappa_{\mathrm{c}}\boldsymbol{B}_{\mathrm{th}} + \sigma_{\mathrm{c}}\boldsymbol{S}_{\mathrm{c}} + \kappa_{\ell}\varphi_{\ell}\boldsymbol{S}_{\ell,x}}{\kappa_{\mathrm{c}} + \sigma_{\mathrm{c}} + \kappa_{\ell}}, \tag{1}$$

where $\boldsymbol{B}_{\mathrm{th}}$ is the thermal source (Planck function), and $\boldsymbol{S}_{\mathrm{c}}$ is the continuum scattering source function as implemented by Fluri & Stenflo (1999). Note that source functions and radiation field are 2-component quantities, e.g. $\boldsymbol{I} = (I, Q)$, $\boldsymbol{B}_{\mathrm{th}} = (B_{\mathrm{Planck}}, 0)$. The opacities κ_{c}, σ_{c}, and κ_{ℓ} represent the continuous absorption coefficient, continuous scattering coefficient, and integrated line absorption coefficient, respectively. The line source function has the form

$$\boldsymbol{S}_{\ell,x} = \frac{(1-\epsilon)}{2\varphi_x} \int_{-\infty}^{+\infty} \int_{-1}^{+1} \hat{\boldsymbol{R}}(x, x'; \mu, \mu')\boldsymbol{I}_{x'}(\mu')\, \mathrm{d}\mu' \mathrm{d}x' + \epsilon\boldsymbol{B}_{\mathrm{th}}, \tag{2}$$

where φ_x represents the normalized Voigt profile, and x and x' denote scattered and incident frequencies, respectively, in standard Doppler units. The collisional thermalization parameter ϵ is obtained from

$$\epsilon = \frac{\Gamma_{\mathrm{I}}}{\Gamma_{\mathrm{R}} + \Gamma_{\mathrm{I}}}, \tag{3}$$

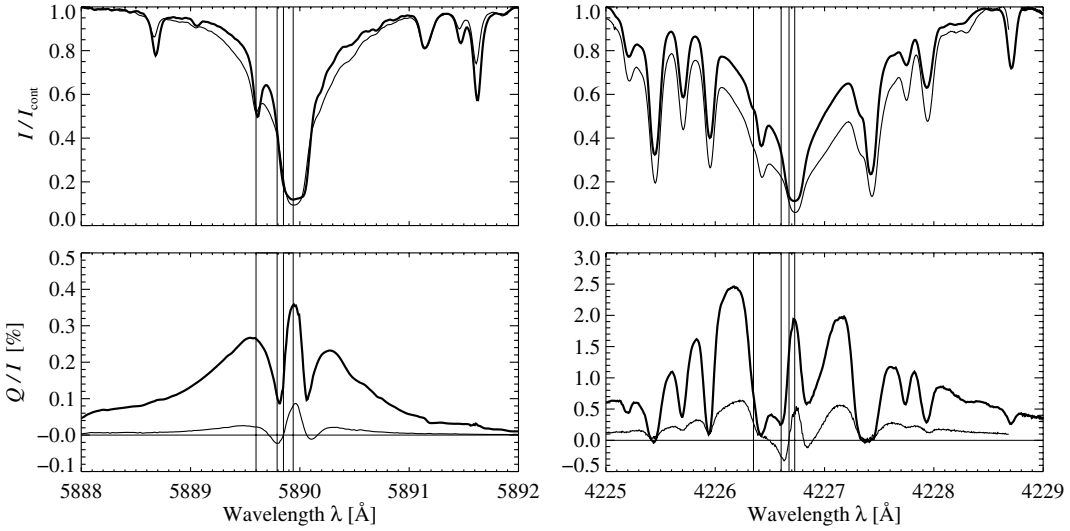

Fig. 1. Observational spectra of Na I D_2 and Ca I 4227 Å obtained with ZIMPOL. Thick lines correspond to $\mu = 0.1$, thin lines to $\mu = 0.5$. The Na I spectra are taken from Stenflo et al. (2000), the Ca I observation at $\mu = 0.1$ from the atlas of Gandorfer (2002). The $\mu = 0.5$ measurement is taken from a recent observing run at IRSOL. The vertical lines in the spectra indicate the selected wavelength positions defined in Table 1. The Ca I line is heavily blended so that the wings are approximated by the envelope of the profile. Note that the chosen continuum position lies outside the plotted spectral windows.

where Γ_R is the radiative de-excitation rate, and Γ_I the inelastic collision rate. We have implemented the redistribution matrix

$$\hat{\boldsymbol{R}}(x,x';\mu,\mu') = \gamma R_{\rm II}(x,x')\,\hat{\boldsymbol{P}}(\mu,\mu',W_{\rm eff}=W_2) + (1-\gamma)\,R_{\rm III}(x,x')\,\hat{\boldsymbol{P}}(\mu,\mu',W_{\rm eff}=k_{\rm c}W_2), \quad (4)$$

with the underlying assumption that frequency and angle redistribution may be separated. The scalar functions $R_{\rm II}$ and $R_{\rm III}$ describe angle averaged frequency redistribution in the standard notation of Hummer (1962). The depth dependent coherence fraction is given by

$$\gamma = \frac{\Gamma_R + \Gamma_I}{\Gamma_R + \Gamma_I + \Gamma_E}, \quad (5)$$

where Γ_E represents the elastic collision rate. The collisional depolarization factor k_c in Eq. (4) is given by

$$k_{\rm c} = \frac{\Gamma_R + \Gamma_I}{\Gamma_R + \Gamma_I + D^{(2)}} \cdot \frac{\Gamma_E - D^{(2)}}{\Gamma_E}, \quad (6)$$

where $D^{(2)}$ is the rate of depolarizing elastic collisions. Note that the factor k_c does not appear in the $R_{\rm II}$-term because by definition this term describes scattering events undisturbed by collisions. For the phase matrix we use the notation defined by

$$\hat{\boldsymbol{P}}(\mu,\mu',W_{\rm eff}) = \hat{\boldsymbol{P}}^{(0)} + W_{\rm eff}\,\hat{\boldsymbol{P}}^{(2)}(\mu,\mu'). \quad (7)$$

The effective polarizability $W_{\rm eff}$ depends in general on the intrinsic polarizability W_2 and on collision rates as stated explicitely in Eq. (4). The matrix $\hat{\boldsymbol{P}}^{(0)}$ represents unpolarized, isotropic scattering, while $\hat{\boldsymbol{P}}^{(2)}$ accounts for scattering of the linear polarization. In absence of magnetic fields the two matrices are given by (cf. Stenflo 1994)

$$\hat{\boldsymbol{P}}^{(0)} = \begin{pmatrix} 1 & 0 \\ 0 & 0 \end{pmatrix}, \quad (8)$$

Table 1. Selected wavelengths in the Na I D_2 and Ca I 4227 Å lines. These wavelengths are used throughout the paper to discuss the prominent features in the polarization profiles.

Domain	Na I D_2	Ca I 4227
continuum	5885.036 Å	4224.612 Å
wing maximum	5889.599 Å	4226.350 Å
minimum	5889.750 Å	4226.603 Å
core rise	5889.850 Å	4226.675 Å
line center	5889.939 Å	4226.727 Å

$$\hat{\boldsymbol{P}}^{(2)} = \frac{3}{8}\begin{pmatrix} \frac{1}{3}(1-3\mu^2)(1-3\mu'^2) & -(1-3\mu^2)(1-\mu'^2) \\ -(1-\mu^2)(1-3\mu'^2) & 3(1-\mu^2)(1-\mu'^2) \end{pmatrix}, \quad (9)$$

where we have chosen the coordinate system such that positive Stokes Q corresponds to linear polarization parallel to the nearest limb. In Sect. 4 we compare our PRD results with CRD calculations. The latter case is implemented by setting $\gamma = 0$ and approximating $R_{\rm III}(x,x')$ by $\varphi_\ell(x)\varphi_\ell(x')$ in Eq. (4).

In our formalism the polarizability W_2 is calculated independently of radiative transfer for a whole multiplet using the density-matrix formalism with the metalevel approach (Landi Degl'Innocenti et al. 1996). Therefore the polarizability W_2 becomes frequency dependent and accounts for lower-level atomic polarization and quantum interferences between fine-structure and hyperfine structure levels. Note that the resulting W_2 is kept fixed and is subsequently inserted into the redistribution matrix in Eq. (4) and thus into the scattering integral in Eq. (2), which was derived for a two-level atom without lower level polarization. A further assumption involved in the computation of W_2 is a constant anisotropy, which does not matter for quantum interferences but influences the treatment of lower-level polarization. This problem was also present in the calculations of Landi Degl'Innocenti (1998). However,

lacking a self-consistent PRD theory of radiative transfer with quantum interferences and optical pumping, the involved simplifications and assumptions seem to be well justified and allow a combination of the advantages of both the integral and density-matrix formalisms as well as an implementation of PRD effects. In the case of the Ca I 4227 Å line the situation is much simpler, because neither hyperfine structure nor lower-level polarization exist and the line is a pure dipole transition with $W_2 = 1 = \text{const}$.

3. Anisotropy of the radiation field

Linear polarization produced in coherent scattering is proportional to the anisotropy of the radiation field, as described by Eq. (2). Therefore, deep insight into the behavior of the anisotropy including its frequency and depth dependence is essential for understanding the emergent polarization profile.

The anisotropy of the radiation field is defined by (e.g. Trujillo Bueno 2001)

$$A = \frac{J^2_0}{J^0_0}, \tag{10}$$

where J^0_0 is the mean intensity and J^2_0 is given by

$$J^2_0 = \int \frac{\mathrm{d}\Omega'}{4\pi} \frac{1}{2\sqrt{2}} (3\mu'^2 - 1) I_{x'}. \tag{11}$$

We have omitted the contribution of Stokes Q, because we neglect the feedback of polarization on intensity. The factor $(3\mu'^2 - 1)$ is taken from the (1, 1)-element of the phase matrix in Eq. (9). The sign of the anisotropy has been chosen such that positive anisotropy translates by coherent scattering into positive Stokes Q, i.e. with our convention into linear polarization parallel to the limb.

In the remainder of this work we will study the polarization profiles at certain selected wavelengths given in Table 1 and indicated as vertical lines in the observations of the Ca I 4227 Å and Na I D_2 lines (Fig. 1). These wavelengths are representative of the different spectral features of the triplet peak. In particular we distinguish between the continuum, the wing maxima, the polarization minima, the core rise, and the line center. We will use these expressions to refer to the selected wavelengths.

In the present section we start with general considerations on the formation of the anisotropy. Then we review briefly the intensity contribution function and source function of chromospheric lines at the selected wavelengths, before we discuss the frequency and depth dependence of the anisotropy.

3.1. Basic considerations: Boundary effects and source function variations

To understand the basic mechanisms affecting the anisotropy we consider three simple academic cases, of which the first and second have been discussed in detail by Trujillo Bueno (2001). Later, in Sect. 3.4, we find that all three cases are relevant for the formation of line polarization at certain depths and frequencies.

The three examples are illustrated in Fig. 2. The rectangles represent a semi-infinite atmosphere, not illuminated from above, with the top of the atmosphere in the upper part of the panels. Arrows indicate the incident radiation at two locations within the atmosphere, the first one close to the upper boundary, where the optical depth $\tau < 1$, the second one deeper in the atmosphere, where $\tau > 1$. The thickness of the arrows scales with the intensity of the incident radiation. Therefore the anisotropy can be inferred from the arrows. Following Trujillo Bueno (2001) we split the contributions to the anisotropy in Eq. (11) into two separate parts corresponding to light coming from the lower ($A^{(\ell)}$) and upper ($A^{(\mathrm{u})}$) hemisphere, respectively.

In case a) we consider an isothermal atmosphere. Deep inside the atmosphere the radiation field is isotropic so that both $A^{(\ell)}$ and $A^{(\mathrm{u})}$ are zero, resulting in zero anisotropy. Above optical depth $\tau = 1$ anisotropy is produced by a purely geometrical or boundary effect, as pointed out by Trujillo Bueno (2001): the intensity from the upper hemisphere is reduced because the photon mean free path starts to exceed the distance to the upper boundary, an effect that is more pronounced the more radial the direction of the incident light. This leads to limb brightening in the upper hemisphere, i.e. $A^{(\mathrm{u})}$ becomes smaller than zero, while the outgoing radiation coming from the lower hemisphere remains isotropic ($A^{(\ell)} = 0$), which makes the overall anisotropy smaller than zero. Closer to the surface the anisotropy increases again towards zero at the upper boundary, because no incoming radiation from above remains.

In case b) we assume a Milne-Eddington atmosphere with the source function given by $S = a + b\tau$. Now, the anisotropy is due to the combined influence of the boundary effect discussed above and the source function gradient. Deep inside the atmosphere upward-going radiation is limb darkened while downward-going radiation is limb brightened due the source function gradient, but the two contributions cancel each other giving zero total anisotropy. When approaching the surface, the boundary effect sets in by further increasing the limb brightening of the downward-going radiation. However, now there is the competing effect of the limb darkened radiation from the lower hemisphere. $A^{(\ell)} > 0$ remains positive when approaching the surface, while $A^{(\mathrm{u})}$ eventually increases again to zero due to the overall drop of the intensity from the upper hemisphere. In general, the resulting anisotropy is therefore zero deep inside the atmosphere, becomes negative around $\tau = 1$, and increases again to positive values closer to the surface. The greater the source function gradient, i.e. the greater the ratio b/a, the more limb darkened the radiation from the lower hemisphere becomes, while the boundary effect stays the same. This reduces the dip in anisotropy around $\tau = 1$ and increases the boundary value at the surface (cf. Fig. 4 in Trujillo Bueno 2001).

In the last case c) we consider an atmosphere with two layers separated by a transparent gap, each layer being isothermal. The deeper layer is assumed to be much hotter and therefore has a higher source term ($S_2 \gg S_1$). Additionally, the thickness of the upper region with S_1 is chosen to be semi-transparent in the vertical direction, but optically thick in more horizontal directions. The gap is introduced only for reasons of analogy with the real situation encountered in Sect. 3.2. Actually, for

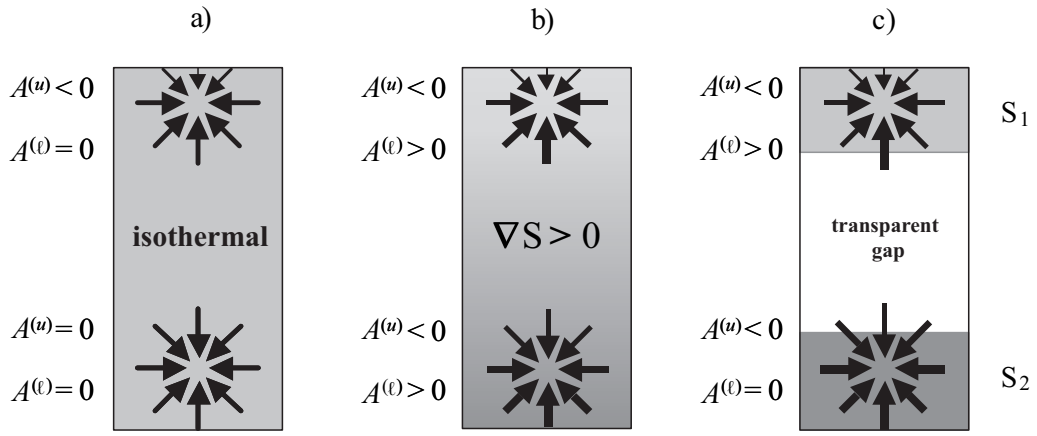

Fig. 2. Three simple academic cases of semi-infinite atmospheres showing possible ways of generating anisotropy of the radiation field. Case **a)**: isothermal atmosphere. The boundary causes negative anisotropy within an optical depth of unity exclusively due to the geometry. Case **b)**: Milne-Eddington atmosphere. The non-vanishing source function gradient ∇S gives an additional (positive) contribution to the anisotropy. Case **c)**: layered atmosphere with a transparent gap. The source function S_1 of the upper, semi-transparent layer is much smaller than the source function S_2 of the lower layer. This results in a strong anisotropy in the upper layer.

this case only the presence of a large step in the source function is relevant. In terms of optical thickness the gap does not exist at all.

The step in the source function gradient produces the same effect in both layers but with opposite sign, namely strongly negative anisotropy in the lower layer and very large positive anisotropy in the upper layer. In the lower layer the situation is analogous to the one at the surface in case a), i.e. the anisotropy in the lower layer becomes strongly negative. In the upper layer the effect of the source function step sets in with the same strength but with opposite sign, i.e. it leads to a strongly positive anisotropy dominated by $A^{(\ell)}$. The situation in the upper layer is very similar to case b) with a very large source function gradient. However, case c) as a whole results in a clearly different anisotropy behavior as compared with case b). While in case b) with a strong gradient the positive contribution dominates at every depth in the atmosphere, the competing effects in case c) are separated geometrically by the gap, leading to positive anisotropy in the upper part and negative anisotropy in the lower part.

In a realistic atmosphere, a complex interplay of many factors is responsible for the appearance and strength of the various effects discussed above. The source function and its gradient vary significantly with depth and frequency in a strong chromospheric line, and the depth of line formation depends on frequency. As we will find in the following all three academic cases a), b), and c) give a good description of the basic situation encountered in different frequency domains of the considered lines. Obviously, we have to look first at the frequency dependence of the contribution function (Sect. 3.2) and the source function (Sect. 3.3) of Stokes I before being able to discuss the anisotropy in chromospheric lines (Sect. 3.4).

3.2. Contribution function of Stokes I

In this subsection we present the contribution function of Stokes I for the Na I D_2 line in the selected wavelength domains. The results for the Ca I 4227 Å line are not shown explicitly since all important qualitative features are the same. The depth and frequency dependence of the contribution function is in principle known. Therefore, we discuss only points relevant for the present work. Usually the main focus has been on disk center calculations, while for our purposes the center-to-limb variation and the detailed frequency dependence are more significant for an understanding of the anisotropy of the radiation field.

Figure 3 shows the contribution function at the selected wavelength points (cf. Table 1) for rays with directions $\mu = 0.1$ (solid) and $\mu = 0.5$ (dotted). As expected, the maximum of the contribution function lies higher for smaller μ because of the larger optical thickness in more horizontal directions, and shifts to higher layers when approaching the line center due to the increasing line opacity.

Of particular interest is the fact that line contributions occur in two main layers, in the photosphere and in the lower chromosphere, respectively, with a gap of about 400 km at the temperature minimum and slightly above (cf. also Stix 2002, Fig. 4.13). The continuum, line wing and minimum form in the photosphere (lower layer), while the line core forms in the chromosphere (upper layer). This gap results from the small temperature around the temperature minimum, which causes the Doppler width and thus the line opacity to decrease. The jump from the lower to the upper layer occurs in a narrow frequency range in the core-wing transition (panel 4 of Fig. 3), where the maximum of the contribution function occurs for $\mu = 0.5$ at height $z \approx 400$ km, and for $\mu = 0.1$ at height $z \approx 1100$ km. In other words, the chromosphere, i.e. the upper layer, is transparent in the radial direction, but optically thick or semi-transparent in more horizontal directions. This situation resembles the layered structure of the atmosphere in the academic case c) of Fig. 2 and leads to a strong increase of the anisotropy in the narrow frequency domain at the core-wing transition, as we will see in Sect. 3.4.

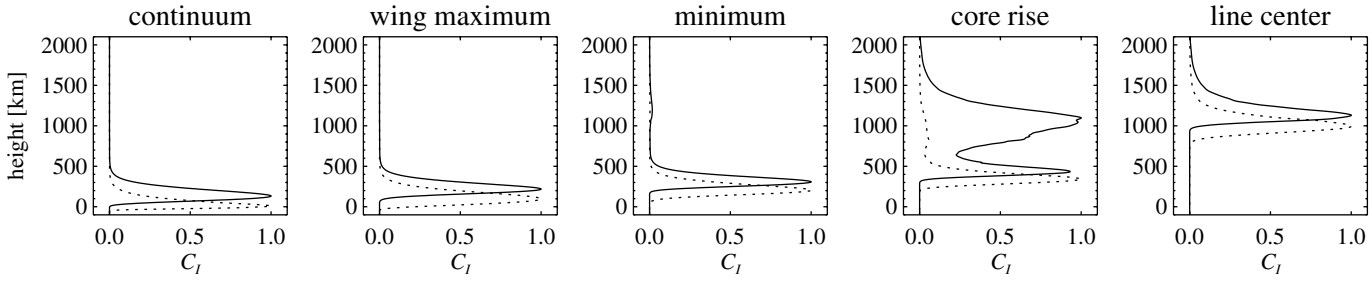

Fig. 3. Contribution function of Stokes I in Na I D_2 for the five selected wavelengths and directions $\mu = 0.1$ (solid) and $\mu = 0.5$ (dotted). Between the heights of 600 km and 1000 km a gap exists with small line contribution only, giving rise to two formation layers. Continuum, wing maximum and polarization minimum form in the lower layer in the photosphere. In the core rise of the line, vertical rays predominantly originate from the deeper region, while horizontal rays form in the upper layer. In this frequency range the upper layer is semi-transparent. In the line core the atmosphere remains opaque up to heights far above the temperature minimum.

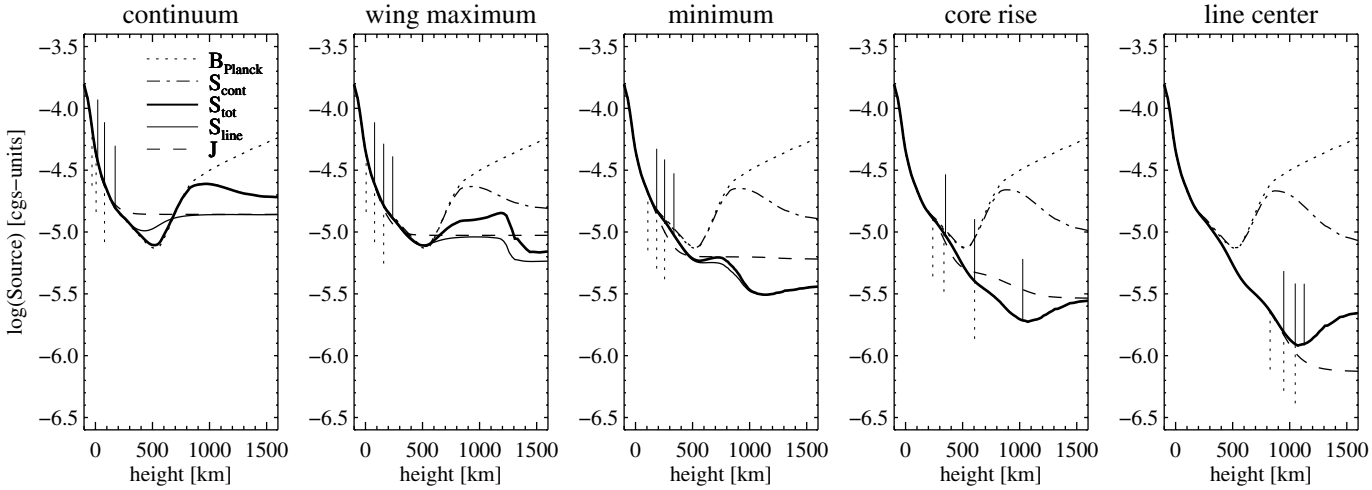

Fig. 4. Depth dependence of the total source function (thick), mean intensity (dashed), Planck function (dotted), continuum source function (dash-dotted), and line source function (solid) of Na I D_2. The three vertical bars indicate heights where the monochromatic optical depth τ_x takes the values 3, 1 and 0.3, respectively, in the directions $\mu = 0.1$ (solid) and $\mu = 0.5$ (dotted). These bars mark the range from where most of the I and Q signals originate.

3.3. Source function gradient of Stokes I

As mentioned previously, the source function and in particular its gradient play a crucial role in the formation of the anisotropy of the radiation field. Therefore, we investigate the source function in this section. Again we show the results for the Na I D_2 line, but all drawn conclusions are also valid for Ca I 4227 Å.

In Fig. 4 the height dependence of the source function is plotted in the selected wavelength domains. We concentrate on the total source function, because it is the most relevant for the formation of the anisotropy. Continuum and line source function, mean intensity and Planck function are shown for reasons of completeness. For a detailed description and the complex interplay of these individual parts of the total source function we refer to Uitenbroek & Bruls (1992).

The total source function $S_{\rm tot}$ (thick line) varies strongly with depth and frequency. However, the layers of line formation, which differ for each wavelength, are the ones that most matter for the anisotropy. Therefore, we can restrict ourselves to these layers, which are determined by the contribution function discussed before. The vertical bars in Fig. 4 indicate the height at which the monochromatic optical depth τ_x has the values 3, 1, and 0.3, which gives a good indication of the layers of line formation. We distinguish between the two directions $\mu = 0.1$ (solid bars) and $\mu = 0.5$ (dotted bars).

From the vertical bars we get a good impression of the total source function gradient within the relevant atmospheric layers. The gradient is steepest in the continuum and drops in the wavelength domains of the wing maximum and in the polarization minimum. The core rise domain again is the exception due to the jump in line formation. The three bars are spread over a much wider atmospheric layer, resulting in a very large source function gradient in terms of optical depth. This situation resembles case c) in Fig. 2 with a large step in the source function combined with a gap in the contribution function. At the line center the source function gradient becomes almost flat.

From Fig. 4 we can expect a decrease in anisotropy from the continuum to the polarization minimum, the largest anisotropy in the core rise domain, and nearly zero anisotropy in the core.

3.4. Height and frequency dependence of the anisotropy

Knowing the contribution and source functions we can now proceed to the interpretation of the radiation field anisotropy.

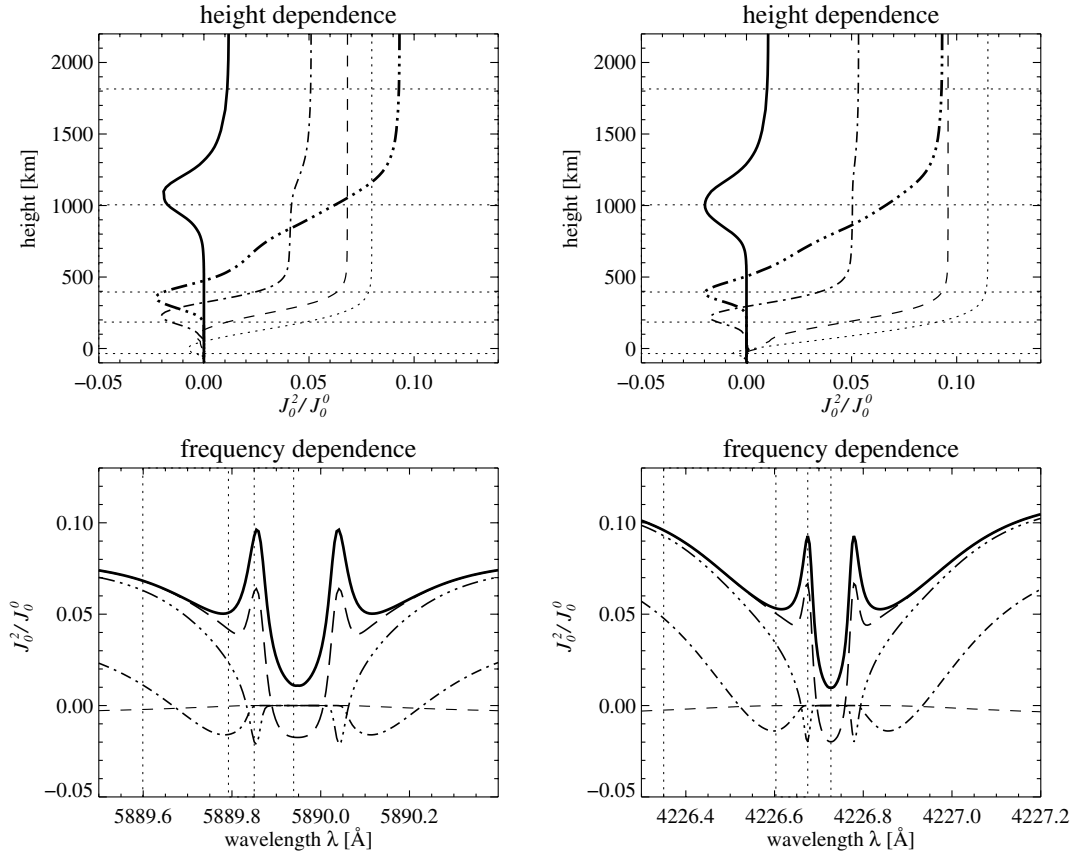

Fig. 5. Height and frequency dependence of the anisotropy for Na I D_2 (left panels) and Ca I 4227 Å (right panels). *Upper panels*: anisotropy as function of height for the selected wavelength domains (Table 1). Solid: line core. Dash-triple-dotted: core-rise. Dash-dotted: polarization minimum. Dashed: wing maximum. Dotted: continuum. Thin horizontal lines denote the position of the selected heights (Table 2). *Lower panels*: anisotropy vs. wavelength for the selected heights. Solid: 1800 km. Dashed thick: 1000 km. Dash-triple-dotted: 400 km. Dashed-dotted: 200 km. Dashed: −40 km. The thin vertical lines give the positions of the selected wavelengths.

Figure 5 shows the anisotropy for both the Na I D_2 (left panels) and the Ca I 4227 Å (right panels) lines. The results for the two lines are very similar. It is however important to compare both lines at this stage because of the arguments regarding the influence of hyperfine structure and lower-level polarization in the Na I D_2 line. In the upper panels of Fig. 5 the height dependence is given for the selected wavelengths (cf. Table 1). The horizontal dotted lines in the upper panels mark five chosen heights in the atmosphere listed in Table 2. For these heights the frequency dependence of the anisotropy is plotted in the lower panels.

The selected atmospheric heights represent different layers relevant for the line formation. The deepest position is below the line and continuum formation region, where the radiation field converges to the Planck function and the anisotropy is zero. In the photosphere, represented by the heights at 200 km and 400 km, the continuum, line wings, and polarization minima form, while around 1000 km the line core originates. Finally, the uppermost position corresponds to the conditions at the top of the atmosphere. There the radiation field is completely decoupled from local conditions so that the anisotropy becomes constant with depth.

Qualitatively, the height dependence of the anisotropy is for most wavelength points consistent with the academic case of a Milne-Eddington atmosphere discussed in Sect. 3.1: deep in the atmosphere the anisotropy is zero, then, moving upward, it decreases due to the boundary effect but rises again in the upper atmosphere (Trujillo Bueno 2001). The details and differences between the wavelength domains will be discussed in the following, starting with the continuum and ending with the line core.

Table 2. Selected height positions in the atmosphere above $\tau_{5000} = 0$. These heights are used in Fig. 5 for plotting the anisotropy.

Description	Height (km)
high atmosphere, decoupled radiation field	1800
lower chromosphere, origin of line core	1000
upper photosphere, origin of minima	400
mid photosphere, origin of line wings	200
deep atmosphere, almost complete thermalization	−40

The anisotropy in the continuum (dotted line, upper panel Fig. 5), wing maximum (dashed), and in the minimum (dot-dashed) can be considered together. The situation corresponds qualitatively to case b) in Fig. 2, the Milne-Eddington atmosphere. The main difference between the three wavelength domains is the gradient of the total source function in the photospheric layers where continuum, wing, and minimum form.

From Fig. 4 we know that the source function gradient around $\tau_x = 1$ is steepest in the continuum and drops towards wing maximum and minimum. Therefore, the effect of the source function gradient wins most clearly in the continuum against the boundary effect. Correspondingly, the anisotropy reaches the highest value in the upper atmosphere, and the drop to negative anisotropy is barely visible, in contrast to the polarization minimum.

In the the Ca I 4227 Å line, the anisotropy becomes more positive in the continuum and wing because of the stronger limb darkening at shorter wavelengths, i.e. because of the larger gradient of the Planck function.

The wavelength domain of the core rise is the most complex. Due to the jump in the contribution function the situation corresponds to the layered atmosphere of case c) in Fig. 2. In the photosphere and up to 700 km the depth dependence of the anisotropy at this wavelength (triple-dotted-dashed line, upper panel Fig. 5) corresponds well to the anisotropy in the polarization minimum and the wing domains: the boundary effect combined with the moderate source function gradient lead to strongly negative anisotropy around 400 km and increasing anisotropy above, which starts to level off at 700 km. Higher in the atmosphere, above the gap in the contribution function, the upper, semi-transparent layer causes a strong increase in anisotropy due to the large difference in the source function between the lower and upper layer. This peak in anisotropy is also well visible in the lower panels of Fig. 5, of course only in the upper atmosphere at 1000 km (long-dashed) and at 1800 km (solid).

In the line core the situation becomes simplified. The gradient of the total source function is almost zero, corresponding to the isothermal case a) in Fig. 2. For the formation of the anisotropy only the boundary effect is significant, i.e. the anisotropy drops clearly to negative values around the line core formation height at 1000 km and rises back towards zero anisotropy at the top of the atmosphere. The marginally positive anisotropy at the top is due to the very small source function gradient.

We should briefly consider the influence of frequency redistribution. Above, we have argued in terms of the academic cases discussed in Sect. 3.1 based on the boundary effect and the source function gradient, implicitly assuming frequency coherence. The beauty of these arguments is that they are sufficient to describe the complex frequency and depth dependence of the anisotropy. In realistic non-LTE calculations frequency redistribution shifts the frequency of photons and thus smears out to some extent the anisotropy features obtained in a purely frequency coherent scenario. The results shown in Fig. 5 were obtained taking PRD into account, but they would change only marginally when assuming CRD. This shows that different frequency redistribution mechanisms are not sufficient to modify the simple, qualitative picture given above.

4. Polarization profile

In this section we discuss the emergent polarization profile separately for the different wavelength domains. Scattering polarization can be mapped to a certain degree from the frequency dependence of the anisotropy A of the radiation field (Rees & Saliba 1982). This becomes apparent when considering the approximate expression

$$\frac{Q}{I} \propto \frac{\boldsymbol{S}_{Q,\mathrm{tot},x}(\tau_x \approx \mu)}{\boldsymbol{S}_{I,\mathrm{tot},x}(\tau_x \approx \mu)} \propto \frac{\sigma_\mathrm{c}\boldsymbol{S}_\mathrm{c} + \kappa_\ell \varphi J^0_0 A W_\mathrm{eff}}{\kappa_\mathrm{c}\boldsymbol{B}_\mathrm{th} + \kappa_\ell \varphi J^0_0}. \tag{12}$$

Note that this equation is not strictly correct mathematically. Stokes Q and I form in general at different depths, and proper frequency redistribution is neglected. The expression however contains the main dependences and is very useful for obtaining the general idea of the origin of the scattering polarization profile.

Frequency redistribution has a large influence on the Q/I profile and has to be included in the following discussion. The CRD and PRD mechanisms determine the frequency window over which the scattering integral in Eq. (2) gives the largest contributions. Therefore we can still base our arguments on the anisotropy but have to account for the selection in frequency due to the relevant redistribution mechanism.

Figure 6 shows the polarization profile of Na I D_2 and the Stokes Q contribution function for different lines of sight and wavelengths. Again the Ca I 4227 Å line gives analogous results and is thus not shown. To illustrate the influence of frequency redistribution we have plotted results computed both with PRD (solid lines) and with CRD (dot-dashed lines).

4.1. Continuum and line wing

Scattering polarization in the line wings (apart from continuum polarization) is only formed in the presence of PRD (Rees & Saliba 1982; Faurobert 1988). In PRD the frequency of a scattered photon shifts typically by one Doppler width, so that a wing photon remains in the line wing and thus increases the degree of polarization in the wing. In CRD, on the other hand, frequencies are redistributed over the whole line profile so that an incident photon with a frequency in the wing has the greatest probability to be emitted in the line core after the scattering process. Therefore, with CRD the line polarization differs from the continuum level only close to the line core.

In the strong chromospheric lines considered here, the wing polarization forms in the photosphere (see Fig. 6). At these layers the coherency fraction γ is of the order of 0.5, i.e. frequency redistribution described by R_II is relevant in about half of the scattering processes. The remaining scattering events are characterized by R_III, which corresponds approximately to CRD, and thus do not contribute to wing polarization.

The increase in polarization from continuum to the wing maximum was correctly described by Rees & Saliba (1982). From Eq. (12) we see that Q scales with φ while I remains almost constant as long as the Planck term dominates. Thus, the polarization increases from the continuum level until the line source term for Stokes I becomes relevant. Note that in the Na I D_2 and Ca I 4227 Å lines the continuum polarization is much smaller than the line polarization.

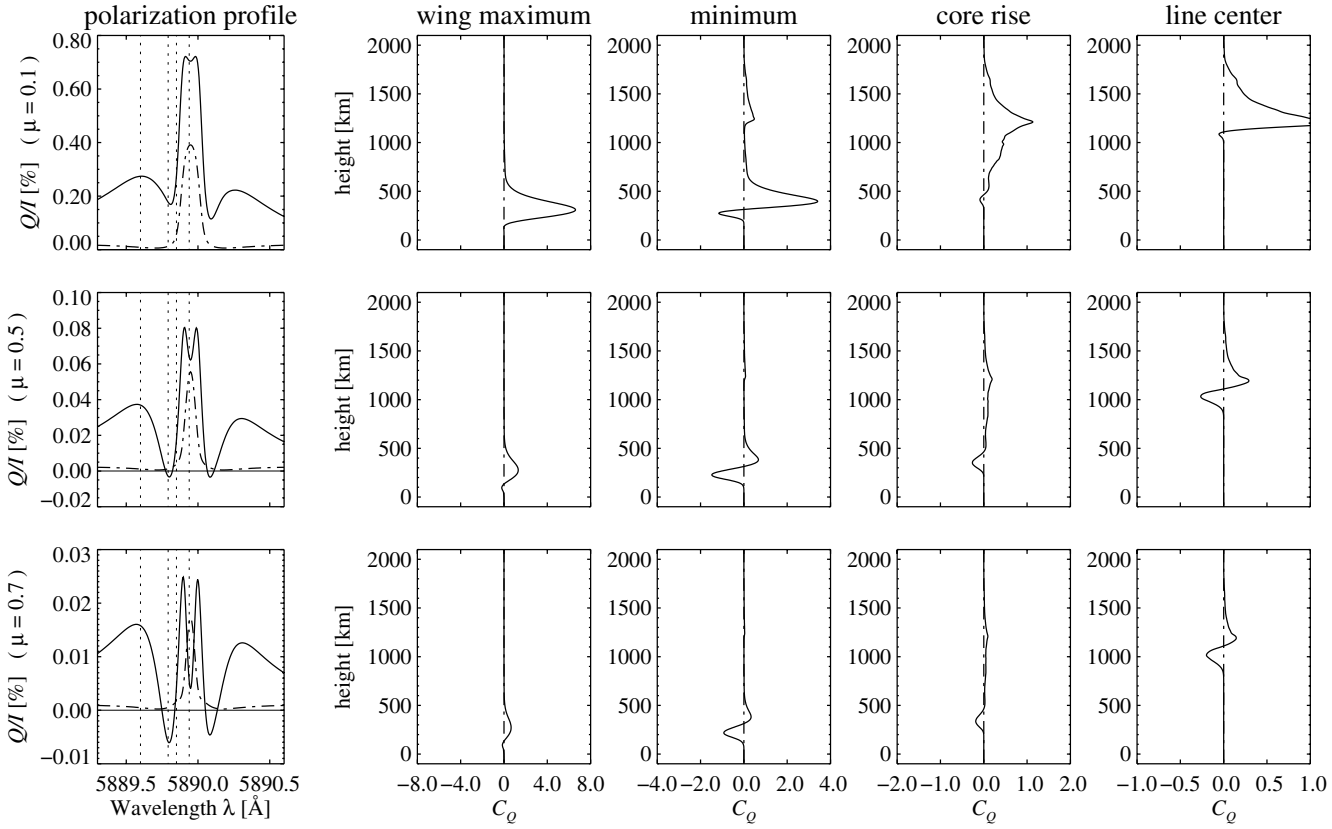

Fig. 6. Calculated polarization profiles and height dependence of the contribution function of Stokes Q for three different angles ($\mu = 0.1$ *upper row*, $\mu = 0.5$ *middle row*, $\mu = 0.7$ *lower row*) and the four selected wavelength domains (continuum omitted). The solid profile curves are for PRD, the dash-dotted for CRD. The results shown are for Na I D_2.

4.2. Polarization minima

The polarization minima are so close to the core that the line source function starts to dominate both in Q and I. Therefore, from Eq. (12), we find that $Q/I \propto AW_{\rm eff}$. With constant anisotropy and $W_{\rm eff}$ we would expect constant polarization over the whole line core, including the minima. This agrees with the calculations of Rees & Saliba (1982) when employing coherent scattering without chromospheric temperature rise.

Obviously, the polarization minima are caused by the smaller anisotropy due to the boundary effect and the smaller source function gradient at the frequencies around the minima. PRD ensures that only narrow frequency windows around the minima contribute to the scattering integral (Faurobert 1988; Faurobert-Scholl 1992), such that the negative parts of the anisotropy carry larger weight, while the positive anisotropy farther in the wings is less important (cf. the lower panels in Fig. 5). Faurobert-Scholl (1992) has attributed the negative anisotropy and thus the polarization minima to the "more efficient trapping" of photons in the horizontal direction close to the limb. This is correct if understood in terms of the boundary effect discussed in Sect. 3, but not that precise. She has also shown that the anisotropy becomes more negative in presence of a chromosphere (Faurobert 1988). Note however, that the total source function barely increases in the lower chromosphere at the wavelengths of the polarization minima. We would like to stress that the boundary effect is a common phenomenon present not only around the polarization minima but at all wavelengths. It is the smaller source function gradient (which in the photosphere is determined by the temperature gradient) combined with the boundary effect, that might be enhanced due to the chromospheric temperature rise, which together reduce the anisotropy and thus the polarization only around the wavelengths of the minima.

The polarization minima exhibit a prominent center-to-limb variation. Close to the limb ($\mu = 0.1$, Fig. 6), the polarization remains positive at the minima, while towards disk center the polarization becomes negative in the minima ($\mu = 0.5$ and $\mu = 0.7$, Fig. 6), in accordance with the observations of Stenflo et al. (2000). This is explained by the different formation heights together with the fact that at these wavelengths the anisotropy is strongly negative in the mid-photosphere and becomes positive in the upper photosphere (Fig. 5). For small μ, the scattering polarization forms higher in the atmosphere, so that only a small portion of the negative anisotropy lies within the formation layer. In a more radial direction (large μ), the polarization originates from deeper layers and fully samples the region with negative anisotropy. Correspondingly, the negative part of the Stokes Q contribution function increases relative to the positive part for larger μ (column of minima, Fig. 6)

In the CRD profiles in Fig. 6 the polarization also decreases to almost zero around the wavelengths of the minima. This effect is not caused by a reduction of the anisotropy, because the distance from the line center is still too large. Rather, it is due to depolarization of the continuum (Fluri & Stenflo 2003) caused

by the line opacity. The same effect is actually present in the PRD profile, but it can be neglected, since the line polarization clearly exceeds the continuum polarization.

Note that polarization minima and line wings are also obtained in isothermal atmospheres (Rees & Saliba 1982; Faurobert 1987, 1988) and are therefore a common feature of PRD radiative transfer. This might sound surprising in view of our arguments given above. The boundary effect is however also present in an isothermal atmosphere, and the total source function gradient depends on both frequency and depth. Combined with PRD this apparently simple academic case already becomes rather complex. It can be explained with the same arguments given here, but a closer examination of the anisotropy and source function is needed.

4.3. Line core

In the line core the polarization is again increasing strongly. The complicated frequency dependence of the anisotropy (Fig. 5) is mapped to polarization but is strongly modified by frequency redistribution.

From the anisotropy we would expect two narrow side peaks around the core and a pronounced dip possibly even to negative values at the very line center. The PRD polarization profiles do indeed exhibit a dip with small side peaks (Fig. 6), while no dip is visible with CRD. However, the dip is not as prominent as one would expect from the anisotropy. Note also that in the Ca I 4227 Å line the dip is much less visible than in Na I D_2. This dip has already been noticed by Faurobert-Scholl (1992). A decrease in polarization at line center was also found by Saliba (1985) for the Ca II K line, but there the situation is not quite comparable, because the intensity profile is itself modified by self-absorption in the core.

The frequency redistribution mechanism is obviously influencing the polarization substantially even in the core. With CRD the frequencies of the scattered photons becomes distributed so strongly that they completely smear out the negative contributions to the polarization at line center and the positive side peaks. Note however that the CRD profiles are only of academic interest, because the density in the lower chromosphere is so low that PRD dominates completely. PRD is often believed to be well represented by CRD in the line core, but the two mechanisms are not identical. With PRD the frequency redistribution is occurring within a sufficiently small frequency range to clearly maintain the structure present in the anisotropy with a dip and side peaks. On the other hand, the smearing effect is also noticeable in the PRD profiles. Without this smearing the negative parts in the Stokes Q contribution function would be much more pronounced at line center (Fig. 6).

Such a central dip has frequently been observed for the Na I D_2 line (Stenflo et al. 2001; Martínez Pillet et al. 2001), but since these observations were made in regions with weak magnetic activity, it is not clear what role the Hanle effect may have played in producing the dip. A central dip has not yet been reported for Ca I 4227 Å observations, and it has not been seen for Na I D_2 observations in the polar regions, where the influence of magnetic fields is expected to be minimal. This apparent observational absence may however be due to insufficient spectral resolution, since previous observations were not designed to properly resolve such narrow spectral features. In addition our numerical calculations show that the strength of the dip depends strongly on atmospheric parameters. For a good test of our radiative transfer modeling and for constraining model atmospheres new polarimetric observations with very high spectral resolution (e.g. 20 mÅ) of both the Ca I and Na I D_2 line cores in non-magnetic regions would be needed.

4.4. Influence of hyperfine structure and lower-level polarization in the Na I D lines

The Na I D_2 line is subject to hyperfine structure and possibly lower-level polarization caused by optical pumping, in contrast to the Ca I 4227 Å line. Only when including both of these effects Landi Degl'Innocenti (1998, 1999) was able to get a good fit to observations. He assumed frequency-coherent scattering and constant anisotropy combined with an unrealistically high value for the lower-level atomic polarization. It however remained questionable whether lower-level atomic polarization could survive in the presence of magnetic field strengths of the order of several gauss. Trujillo Bueno et al. (2002) have shown that the alignment in the ground level $S_{1/2}$ of Na I becomes practically negligible for magnetic field strengths greater than 10 G, independent of the field orientation. Without lower-level atomic polarization the mechanism proposed by Landi Degl'Innocenti (1998, 1999) would not produce a central polarization core. However, in view of his first explanation of scattering polarization in the Na I D lines, we need to assess the influence of hyperfine structure and lower-level atomic polarization in these lines.

In the left panel of Fig. 7 the polarizability W_2 is shown for three cases involving (i) only fine-structure (solid); (ii) fine-structure and hyperfine structure (dotted); and (iii) fine-structure, hyperfine structure plus lower-level atomic polarization (dashed). All cases refer to zero magnetic field. The three cases differ in W_2 only within the line core, while the slower overall gradient, including the sign reversal, which is due to quantum interferences between the fine-structure components, is unaffected. The polarizability W_2 remains nearly zero in the core of D_1, because we have selected more realistic values of the anisotropy that is actually present in the core formation region, in contrast to the ad hoc assumptions of Landi Degl'Innocenti (1998, 1999).

The emergent polarization in Na I D_2 for the three cases of W_2 is plotted in the right panel of Fig. 7. Big differences are only found in the line core, while the minima differ only marginally and the line wings coincide. Since scattering polarization in first order scales linearly with W_2, we find the largest core peak when considering only fine-structure, while the smallest core peak results for fine-structure and hyperfine structure but neglecting lower-level polarization (see also Landi Degl'Innocenti 1998). The triplet peak structure is maintained in all cases. This is a strong indication that radiative transfer involving PRD and the related frequency and depth dependence of the anisotropy are mainly responsible for the

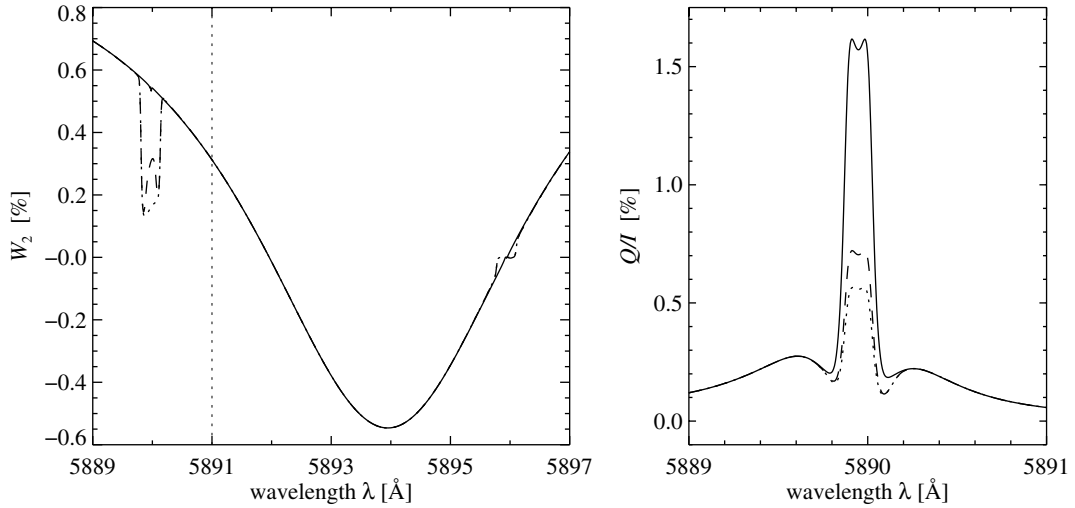

Fig. 7. Influence of hyperfine structure and lower-level atomic polarization on the emergent polarization profile. Three cases are compared: only fine-structure (solid), fine-structure and hyperfine structure (dotted), and fine-structure, hyperfine structure plus lower-level polarization (dashed). The polarizability W_2 (*left panel*) is plotted for both the Na I D_1 and D_2 lines, while the emergent polarization (*right panel*) is only given for D_2 in the direction $\mu = 0.1$. The vertical line in the left panel indicates the right border of the wavelength window selected for plotting the polarization profile in the right panel. Note that a triplet structure is obtained for all the cases.

triplet structure in Na I D_2, as well as in the Ca I 4227 Å line. Hyperfine structure and lower-level polarization merely lead to a modification of the core polarization, which is of course relevant in quantitative diagnostics, but do not alter the qualitative picture.

As concerns the Na I D_1 line, the polarization in the line wings and in the minima might also be explained by PRD radiative transfer, as long as fine-structure interferences are accounted for in W_2. Note that the density-matrix formalism applied to non-magnetic atmospheres gives antisymmetric profiles in the line core (Landi Degl'Innocenti 1998, 1999) in contrast to observations (e.g. Stenflo & Keller 1997; Stenflo et al. 2000). When the scattering polarization modeling is carried out without accounting for radiative transfer effects, then it is only in the presence of a magnetic field that the antisymmetric profile can be suppressed (Trujillo Bueno et al. 2002). With our PRD radiative transfer it is much easier to obtain the correct symmetry in the line core, i.e. the symmetric minima, because we correctly account for the frequency (and depth dependence) of the anisotropy, which is symmetric with respect to the line center and has the smallest values at the frequencies of the polarization minima. Nonetheless, the observed D_1 core polarization remains enigmatic and beyond reach of the present modeling.

5. Conclusions

Our strategy for modeling scattering polarization consists of two steps and assumes that the degree of polarization is sufficiently small to neglect its influence on the intensity. In the first step intensity, opacities, and collision rates are computed using the multi-level RH-code developed by Uitenbroek (2001). In the second step scattering polarization with PRD is calculated iteratively only for the transitions of interest, keeping intensity, opacities, and collision rates fixed. We do this by using the line source function expression in Eq. (2), which is valid for a two-level atomic model with unpolarized ground level. Quantum interferences and optical pumping are accounted for in Eq. (2) by using a frequency dependent polarizability W_2, calculated via the density-matrix theory.

This code package has allowed us to obtain an explanation of the triplet peak structure of the scattering polarization profile that is often observed in strong chromospheric lines. Our interpretation is based on key considerations in terms of the anisotropy of the radiation field (Trujillo Bueno 2001) and the frequency redistribution mechanism (Faurobert-Scholl 1992).

The complicated frequency and depth dependence of the anisotropy is governed by two competing effects, namely a boundary effect causing limb-brightening of the radiation field in the upper hemisphere and the total source function gradient causing limb-darkening in the lower hemisphere. In the continuum and line wings the effect of the source function gradient clearly wins. In the upper photosphere, where the polarization minima form, the source function gradient gets smaller and the boundary effect becomes more prominent, leading to a smaller anisotropy with negative values in the upper photosphere. A prominent peak in the anisotropy occurs in the chromosphere in a narrow frequency range at the edge of the line core. It results from a gap of about 400 km in the contribution function, combined with a strong drop in the total source function between the two layers. At line center the total source function becomes almost flat in the lower chromosphere where the core originates. Therefore the boundary effect dominates and reduces the anisotropy again.

The emergent polarization can be mapped from the depth and frequency dependence of the anisotropy combined with the proper frequency redistribution. In the far wing the polarization increases, because Stokes Q scales with the line profile φ, while the intensity is still dominated by the continuum and remains almost constant. Closer to the line center, the anisotropy

governs the polarization profile and causes the various features: the minima due to the dominating boundary effect, the strong increase in polarization at the edge of the core, which forms around the gap in the contribution function, and a dip in the line center. The core peaks and the dip are smeared due to frequency redistribution, which is dominated by PRD in the core. The polarization wings are only present with PRD, which governs half of the scattering events in the upper photosphere, where the wings originate.

In particular, we have shown that the triplet structure in Na I D_2 is mainly due to radiative transfer effects with PRD, as is the Ca I 4227 Å line. Hyperfine structure and lower-level polarization only modify the degree of polarization in the line core without significantly altering the minima and wings.

The interpretation given in the present paper is generally valid for chromospheric lines, although our discussion has focused on two typical examples, the Na I D_2 and the Ca I 4227 Å lines. If the degree of continuum polarization is comparable to the line polarization, then depolarization of the continuum also has to be taken into account. This situation is often encountered in the blue and near UV (see Gandorfer 2002, 2004) because polarization in the continuum is much stronger towards the blue (Fluri & Stenflo 1999; Stenflo 2005). Then, in first approximation, the line polarization has to be added to the depolarized profile that would be obtained with zero intrinsic polarizability W_2 (Fluri & Stenflo 2003). Because the continuum is depolarized to nearly zero in the line core, this can result in polarization profiles with a triplet structure, in which the core polarization does not even exceed the continuum value, while the line wings suffer less from depolarization and are significantly more polarized than the continuum.

Our modeling strategy and the gained insight into the scattering polarization of chromospheric lines will allow us to fit observational profiles of lines such as Na I D_2 and Ca I 4227 Å. We plan to explore the diagnostic potential of these two lines for constraining model atmospheres and for studying the structure of the magnetic field via the Hanle effect.

Acknowledgements. We are indebted to Han Uitenbroek who provided us with his wonderful RH code for Non-LTE radiative transfer, which we have used to compute Stokes I. Joachim Klement has calculated the wavelength dependence of the polarizability W_2, which was needed for studying the influence of hyperfine structure and lower-level atomic polarization on the Na I D profiles. We thank Achim Gandorfer for supplying his atlas of scattering polarization in electronic form. We also acknowledge the cordial support of Daniel Gisler, Michele Bianda and Renzo Ramelli at IRSOL for some of the Ca I 4227 Å measurements used in this work. And we are grateful for the suggestions of the referee helping to improve the manuscript.

References

Bommier, V. 1997a, A&A, 328, 706
Bommier, V. 1997b, A&A, 328, 726
Bruls, J. H. M. J., Rutten, R. J., & Shchukina, N. G. 1992, A&A, 265, 237
Carlsson, M. 1986, Upps. Astron. Obs. Rep., 33
Faurobert, M. 1987, A&A, 178, 269
Faurobert, M. 1988, A&A, 194, 268
Faurobert-Scholl, M. 1992, A&A, 258, 521
Faurobert-Scholl, M. 1994, A&A, 285, 655
Fluri, D. M., & Stenflo, J. O. 1999, A&A, 341, 902
Fluri, D. M., & Stenflo, J. O. 2003, A&A, 398, 763
Fluri, D. M., Holzreuter, R., Klement, J., & Stenflo, J. O. 2003, in Solar polarization, proc. 3rd SPW, ed. J. Trujillo Bueno & J. Sánchez Almeida, ASP Conf. Ser., 307, 263
Fontenla, J. M., Avrett, E. H., & Loeser, R. 1993, ApJ, 406, 319
Gandorfer, A. 2000, The Second Solar Spectrum, Vol I: 4625 Å to 6995 Å (Zurich: VdF), ISBN No. 3 7281 2764 7
Gandorfer, A. 2002, The Second Solar Spectrum, Vol II: 3910 Å to 4630 Å (Zurich: VdF), ISBN No. 3 7281 2844 4
Gandorfer, A. 2004, The Second Solar Spectrum, Vol III (Zurich: VdF), in preparation
Hummer, D. G. 1962, MNRAS, 125, 21
Ivanov, V. V. 1991, in Stellar Atmospheres: Beyond Classical Models, NATO ASI Series C 341, ed. L. Crivellari, I. Hubeny, & D. G. Hummer (Dordrecht: Kluwer), 81
Kneer, F. 1975, ApJ, 200, 367
Landi Degl'Innocenti, E. 1998, Nature, 392, 256
Landi Degl'Innocenti, E. 1999, in ASSL, Vol. 243, Solar Polarization, Proc. 2nd SPW, ed. K. N. Nagendra, & J. O. Stenflo (Dordrecht: Kluwer), 61
Landi Degl'Innocenti, E., Landi Degl'Innocenti, M., & Landolfi, M. 1996, in Forum THEMIS: Science with THEMIS, ed. N. Mein, & S. Sahal-Bréchot (Paris Obs. Publ.), 59
Manso Sainz, R., & Trujillo Bueno, J. 2003, Phys. Rev. Lett., 91, 111102
Martínez Pillet, V., Trujillo Bueno, J., & Collados, M. 2001, in Advanced Solar Polarimetry – Theory, Observations, and Instrumentation, ed. M. Sigwarth, ASP Conf. Ser., 236, 133
Povel, H. P. 1995, Opt. Eng., 34, 1870
Rees, D. E., & Saliba, G. J. 1982, A&A, 115, 1
Rybicki, G. B., & Hummer, D. G. 1991, A&A, 245, 171
Rybicki, G. B., & Hummer, D. G. 1992, A&A, 262, 209
Saliba, G. J. 1985, Sol. Phys., 98, 1
Stenflo, J. O. 1994, Solar Magnetic Fields (Dordrecht: Kluwer)
Stenflo, J. O. 2002, in Astrophysical Spectropolarimetry, ed. J. Trujillo Bueno, F. Moreno Insertis, & F. Sánchez, Lectures given at XII Canary Islands Winter School of Astrophysics (Cambridge: Cambridge University Press), 55
Stenflo, J. O. 2005, A&A, 429, 713
Stenflo, J. O., Gandorfer, A., & Keller, C. U. 2000, A&A, 355, 781
Stenflo, J. O., Gandorfer, A., Wenzler, T., & Keller, C. U. 2001, A&A, 367, 1033
Stenflo, J. O., & Keller, C. U. 1996, Nature, 382, 588
Stenflo, J. O., & Keller, C. U. 1997, A&A, 321, 927
Stix, M. 2002, The Sun, 2nd edn. (Berlin: Springer)
Trujillo Bueno, J. 2001, in Advanced Solar Polarimetry – Theory, Observations, and Instrumentation, ed. M. Sigwarth, ASP Conf. Ser., 236, 161
Trujillo Bueno, J., Casini, R., Landolfi, M., & Landi Degl'Innocenti, E. 2002, ApJ, 566, L53
Uitenbroek, H. 2001, ApJ, 557, 389
Uitenbroek, H., & Bruls, J. H. M. J. 1992, A&A, 265, 268